2020

Infragravity wave generation on shore platforms: Bound long wave versus breakpoint forcing

Poate, Timothy G.

Infragravity wave generation on shore platforms: bound long wave *versus* breakpoint forcing

Tim Poate*, Gerd Masselink*, Martin J. Austin[1], Kris Inch[2], Mark Dickson[3] and Robert McCall[4]

Correspondence to: *Coastal Processes Research Group, School of Biological and Marine Sciences, University of Plymouth, Plymouth, UK. E-mail: Timothy.poate@plymouth.ac.uk

[1]School of Ocean Sciences, Bangor University, Wales.

[2]Environment Agency, UK

[3]School of Environment, The University of Auckland, New Zealand.

[4] Deltares, Boussinesqweg 1, 2629 HV, Delft, Netherlands

Abstract

Shore platforms are ubiquitous morphological features along rocky coastlines and display a spectrum of forms from gently-sloping to sub-horizontal with a low tide cliff. They generally front eroding coastal cliffs and play an important natural coastal protection role by dissipating wave energy, especially during energetic wave conditions. Sea-swell wave energy dissipates during wave breaking, but the transfer of incident wave energy to lower frequencies, resulting in infragravity waves, can enable significant amounts of wave energy to persist up to the shoreline. This residual wave motion at the shoreline can carry out geomorphic work, for example by directly impacting the cliff face, but also for removing cliff-toe debris. There are two main mechanisms for generating infragravity wave motion – group bound long waves and breakpoint forcing – and it is not known which of these mechanisms operate on shore platforms. Here we show, using field data collected at a sloping platform in England and a sub-horizontal platform in New Zealand, and supported by numerical modelling, that the group bound long wave mechanism is most important on sloping platforms, whereas breakpoint

forcing dominates on sub-horizontal platforms. Our results also suggest that the infragravity wave motion on the sloping platform is somewhat more energetic than that on the sub-horizontal platform, implying that the latter type of platform may provide better protection to coastal cliffs. However, site-specific factors, especially platform elevation with respect to tidal level and platform gradient, play a key role in wave transformation processes on shore platforms and more field data and modelling efforts are required to enhance our understanding of these processes, especially collected under extreme wave conditions (H_s > 5 m).

1. Introduction

Shore platforms exist within a continuum of forms and are typically observed as (quasi-) horizontal or low gradient ($\tan\beta$ < 0.05) rocky surfaces that occur within or close to the intertidal zone of rocky coasts and are commonly backed by cliffs (Trenhaile, 1987; Sunamura, 1992). The surface of shore platforms ranges from very smooth (like a sandy beach) to very rough and depends on geological factors such as the lithology and stratigraphic characteristics of the bed. Shore platforms are of particular interest to coastal scientists as they directly control the transformation of waves propagating across its surface (e.g., Farrell et al., 2009; Ogawa et al., 2011; Poate et al., 2018), and thus the amount of wave energy reaching the base of coastal cliffs. In turn, this is important in driving coastal cliff recession rates, but rock platforms also provide key evidence for the age, inheritance and mode of development of rocky coasts. Although existing across a spectrum of forms, two end-member types of shore platform have been commonly described in previous studies (e.g., Sunamura, 1992): Type A platforms are gently sloping ($\tan\beta \approx 0.01$–0.05) and usually extend into the sub-tidal zone and Type B platforms are sub-horizontal with a low tide cliff or reef-type feature, the upper part of which can sometimes be seen at low tide (Kennedy, 2016). Shore platform type appears

predominantly controlled by tidal range (Trenhaile, 1987) with sloping platforms typical of large tidal environments (mean spring tidal range > 2 m) and sub-horizontal platforms more common in regions with a small tidal range (mean spring tidal range < 2 m). However, the balance of rock resistance versus wave force is also highly significant (Sunamura, 1992) and sea level history and morphological inheritance also provide important controls on shore platform geometry (e.g., Stephenson et al., 2017).

Infragravity waves are low frequency (0.005–0.04 Hz; 20–200 s) waves that can dominate the spectrum of water motions and sediment transport processes within the inner surf zone (Bertin et al., 2018). There are two widely accepted mechanisms for the generation of infragravity waves, both related to the variation in sea-swell energy induced by wave groups. The first theory for infragravity wave generation was proposed by Biesel (1952), and later by Longuet-Higgins and Stewart (1962) and Hasselmann (1962), who demonstrated theoretically that the modulation of short wave height by wave groups induces a variation in water level causing it to become depressed under groups of large waves, and enhanced where the sea-swell waves are smaller. This variation in water level creates a second-order wave that is ‘bound’ to the wave groups. The bound infragravity wave propagates at the group velocity and has the same wavelength and period as the wave groups, but is 180° out of phase (i.e., the trough of the bound infragravity wave is coincident with the largest waves in the wave group). It is commonly assumed that the bound long wave is released by short-wave breaking and continues to propagate to the shore as a free wave (e.g., Masselink, 1995; Inch et al., 2017). The second generation mechanism, proposed by Symonds et al. (1982), is the time-varying breakpoint in which freely propagating infragravity waves are generated as dynamic set-up/down oscillations as a result of the spatially fluctuating breakpoint of different sized wave groups. According to this mechanism two infragravity waves are generated, both originating at the sea-swell wave

breakpoint and with the same frequency as the wave groups: a set-up wave propagating to the shore (in phase with wave groups) and a set-down wave travelling out to sea (in anti-phase with wave groups).

Laboratory studies have demonstrated that the relative importance of the two generation mechanisms is largely controlled by the beach slope, with bound infragravity waves dominating on mild sloping beaches, and steeper beaches being more conducive to breakpoint generated infragravity waves (e.g., Battjes et al., 2004; Van Dongeren et al., 2007). In addition to bed slope, sea-swell wave steepness has also been shown to have an influence on the generation of infragravity waves (Baldock and Huntley, 2002; Baldock, 2012).

Energetic infragravity wave motions have been suggested as a mechanism to perform geomorphic work, for example by directly impacting the cliff face, and for removing cliff-toe debris (Dickson et al., 2013). Additionally, infragravity waves may increase the level of sea-swell energy at the base of cliffs backing shore platforms by reducing short-wave dissipation through the increase in the local water depth under the infragravity wave crests (i.e., relatively large sea-swell waves ‘ride’ the infragravity wave crests). However, to date, detailed infragravity wave studies have focused primarily on sandy beaches.

Some of the data presented here have previously been used to quantify incident wave dissipation and platform roughness effects (Poate et al., 2016, 2018) and to model incident and infragravity wave signals (McCall et al., 2017), however, prior to these, few published studies have focused on infragravity wave transformation over rocky shore platforms. Beetham and Kench (2011) undertook two field experiments on sub-horizontal shore platforms in New Zealand, however, the study was relatively modest in its analysis and experimental set-up as

data were only collected by five pressure sensors deployed for up to 36 hours, and wave conditions were low-moderate with maximum offshore wave heights not exceeding 1.5 m. The results of this study were mostly consistent with those from sandy beaches, with infragravity wave height linearly dependent on the offshore sea-swell wave height and increasing shoreward with a maximum infragravity wave height of 0.20 m close to shore. Infragravity wave shoaling, quantified as the change in wave height from the platform edge to the cliff toe, was strongest on the wider of the two platforms. A shoreward increase in infragravity wave height and the increasing significance of infragravity energy relative to sea-swell energy on the inner platform, analogous to dissipative sandy beaches, has also been observed on other sub-horizontal shore platforms in New Zealand and in Australia by Marshall and Stephenson (2011) and Ogawa et al. (2011, 2015).

Coral reefs have a morphology that is analogous to sub-horizontal shore platforms, with a relatively horizontal reef flat and a low tide reef step, and have been the subject of several infragravity wave studies (e.g., Lugo-Fernandez et al., 1998; Brander et al., 2004; Pomeroy et al., 2012; Pequignet et al., 2014; Cheriton et al., 2016; Masselink et al., 2019). Coral reefs exist primarily in microtidal regions and have a large bed roughness, and thus friction coefficient, compared to sandy beaches. On a fringing reef in Western Australia, Pomeroy et al. (2012) found that the water motion shoreward of the reef crest was dominated by infragravity waves and that the dominant generation mechanism of the infragravity waves was the time-varying breakpoint at the steep reef crest. This was supported by numerical simulations and is consistent with the theory that breakpoint-generated infragravity waves are more prevalent in steep sloping regimes. The efficiency of the time-varying breakpoint for infragravity wave generation was also observed on coral reefs by Pequignet et al. (2009, 2014) and Becker et al. (2016), and in numerical modelling by Van Dongeren et al. (2013) and Masselink et al. (2019).

Whilst a number of studies have investigated infragravity waves on sub-horizontal shore platforms and similar coral reefs, there are few studies from sloping shore platforms. In a study of wave transformation at five sloping shore platforms around the UK, Poate et al. (2018) observed the total infragravity energy to either remain constant or decrease in the shoreward direction through bed roughness. This characteristic of infragravity waves on rocky platforms, generated by bound wave theory, was supported by Jager (2016), based on the analysis of the field data collected on one of these sloping platforms and supported by XBeach numerical modelling. Recently, an approximate 10 % increase in total infragravity energy was observed across a sloping platform in a macro-tidal setting by Stephenson et al. (2018); however, low-energy wave conditions, measurements at only three cross-shore locations and a largely qualitative analysis limit the ability of their study to elucidate more fully the geomorphic significance of infragravity waves on such platforms.

This paper investigates and compares the generation and transformation of infragravity waves on contrasting sub-horizontal and sloping shore platforms. Field data from a sub-horizontal platform at Leigh, New Zealand, and a sloping platform at Lilstock, UK, are analysed and complimented by numerical modelling using the XBeach model (phase-resolving). The specific objectives of this study are to: (1) assess the relative importance of the bound wave and the time-varying breakpoint theories of infragravity wave generation on the two platforms; (2) investigate and quantify the transformation of infragravity energy across the platforms; and (3) discuss the geomorphic implications of the findings.

2. Methodology

153 2.1 Site description

154

155 Data presented in this paper originate from two field sites: Lilstock (LST) in Somerset, UK,
156 and Tatapouri (TAT) on the east coast of the North Island in New Zealand (Figure **1**). Both
157 sites are part of a larger project looking at wave transformation across rocky platforms, with
158 data from LST presented in Poate et al. (2016, 2018) and McCall et al. (2017). LST experiences
159 macrotidal conditions, with a mean spring range of 10.7 m, and is characterised by a wide (300
160 m), rather smooth and uniformly sloping platform ($\tan\beta = 0.021$). The platform at TAT has a
161 microtidal regime with a 1.4 m mean spring range and is characterised by two distinct slopes
162 with a smooth, upper sub-horizontal section ($\tan\beta = 0.0004$) that extends ~150 m before a break
163 in slope where the profile drops away more rapidly ($\tan\beta = 0.002$) over the lower 150 m. The
164 profiles presented in Figure **1** show the surveyed intertidal portion of the survey area. Extended
165 profiles, highlighting the steep gradient at the edge of the platform at TAT, are presented later
166 in Section 3.3.

167

168 The site at LST is located on the southern side of the Bristol Channel, orientated north, making
169 it relatively sheltered from the dominant south-westerly waves moving in from the North
170 Atlantic. The profile itself is composed of sub-horizontal, c. 0.4-m thick mudstone beds which,
171 through variable exposure and erosion, results in pools and shallow channels (Figure **2c**). The
172 field site at TAT is located on the east coast of the North Island exposed to the Pacific Ocean
173 with incident swell approaching from the south-east (Ogawa et al., 2011). The wide, sub-
174 horizontal platform is dominated by siltstone interbedded with weathered sandstone, which
175 leaves shallow pools and crevices (Figure **2a**). Due to the sub-horizontal bedding planes at both
176 sites, the shore platform surfaces are relatively smooth, minimising frictional wave energy
177 dissipation during wave transformation (cf., Poate et al., 2018).

2.2 Data collection

For each site, a detailed topographic survey was undertaken across the intertidal platform using RTK GPS (LST) and a total station (TAT). Each dataset was transformed onto a local coordinate system as shown in Figure **1**. To provide a comparison of platform roughness, the standard deviation was calculated for a detrended profile using a 5-m moving window. The mean value of this is presented in Figure **1** and shows that LST (0.08 m) exhibited a slightly larger mean value compared TAT (0.06 m), and is hence somewhat rougher.

Hydrodynamic data were collected over eight tides from the 8th December 2014 at LST and over six tides from the 24th February 2016 at TAT. At each site, a linear array of RBR Solo pressure sensors (15 at LST and 14 at TAT) were housed within steel tubes (0.23 m long) and fixed to the platform surface using bolts or heavy weights. The sensors logged continuously at 8 Hz and were evenly spaced across the platforms between the low- and high-water lines. Each sensor was surveyed in position using the GPS or total station for vertical precision.

At TAT, a 1200 kHz Teledyne Workhorse ADCP was deployed on the seabed (looking up) ~300 m from the edge of the platform in 8–10 m water depth to measure the nearshore wave climate. The ADCP was configured for burst sampling, recording 2400 samples at a rate of 2 Hz every 20 minutes. At LST, offshore wave conditions were not available and therefore the outermost PT has been used to represent boundary conditions (when this PT was outside the

surf zone). Table **1** provides a summary of the experimental set-up and platform morphology associated with the two field experiments.

2.3 Analysis methods

The local barometric pressure logged when each pressure sensor was exposed at low water was used to convert the absolute pressure to water surface elevation, and linear wave theory was used to correct for depth attenuation. The results presented herein are based on the analysis of ~17-min data segments (8192 data points), which provided a suitable compromise between tidal stationarity and being able to obtain representative statistical parameters. Bursts that were found to be intermittently wet and dry were excluded from analyses.

Auto-spectra were computed using Hanning-windowed, 50% overlapping segments of 2048 points, providing 12 degrees of freedom (Nutall, 1971) and a frequency resolution df of 0.0039 Hz. Infragravity (0.005–0.05 Hz) and sea-swell (0.05–0.33 Hz) significant wave heights (H_{inf} and H_{ss}, respectively) were calculated as

$$H_{inf} = 4\sqrt{\int_{0.005}^{0.05} E(f)df} \qquad (1)$$

and

$$H_{ss} = 4\sqrt{\int_{0.05}^{0.33} E(f)df} \qquad (2)$$

where $E(f)$ is the spectral density at frequency f. The transition frequency of 0.05 Hz between infragravity and sea-swell waves was selected to be consistent with most previous studies and also corresponds to the spectral valley present in the spectra for the majority of bursts. The high

223 frequency sea-swell cut-off of 0.33 Hz corresponds to an attenuation level of >80% at the most
224 seaward pressure sensor during high tide at LST, and thus higher frequencies could not be
225 resolved confidently.
226
227 The infragravity wave generation mechanism at the two study sites was investigated using
228 cross-correlation analysis between the infragravity time series and the wave group envelope.
229 This technique considers the relationship between two time series with zero mean by applying
230 a time shift to one of the series and has been widely used in infragravity wave research (e.g.,
231 Masselink, 1995; Janssen et al., 2003; Pomeroy et al., 2012; Ruju et al., 2012; Inch et al., 2017;
232 Masselink et al., 2019). The infragravity and sea-swell time series (η_{inf} and η_{ss}, respectively)
233 were calculated using a frequency domain filter whereby the discrete Fourier transformation of
234 the total water surface elevation time series is multiplied by a filter function that has a value of
235 unity at the passband frequencies and zero at all other frequencies, before undergoing an
236 inverse Fourier transformation back into the time domain. The wave group envelope $A(t)$ was
237 calculated following the method of List (1991) as

$$A(t) = \frac{\pi}{2}|\eta_{ss}(t)|_{low} \qquad (3)$$

238 where subscript low indicates a low pass filter of frequency 0.05 Hz, and |..| represents the
239 modulus. The wave group envelope reflects the modulation of sea-swell amplitude on the time
240 scale of wave groups.
241
242 The cross-correlation is expressed as

$$r(\tau) = \frac{\langle \eta_{inf}(t)A(t+\tau)\rangle}{\sigma_{\eta_{inf}}\sigma_A} \qquad (4)$$

243 where τ is a time shift, $\langle . . \rangle$ denotes a time-averaging operator, and $\sigma_{\eta_{inf}}$ and σ_A are the standard
244 deviations of η_{inf} and A, respectively. If the infragravity waves are predominantly bound to

245 the short-wave groups, then the cross-correlation coefficient at a time lag of zero r_0 will
246 approach -1 because the two time series will theoretically be 180° out of phase. The 95%
247 confidence intervals on the zero correlation, calculated following Garrett and Toulany (1981)
248 and Jenkins and Watts (1968), are ±0.02 at LST and ±0.04 at TAT, respectively.
249
250 The grouped nature of the sea-swell waves is investigated further by calculating the groupiness
251 factor GF, proposed by List (1991), as

$$GF = \frac{\sqrt{2var[A(t)]}}{\overline{A}(t)} \qquad (5)$$

252 where var is the variance and the overbar represents the mean. The groupiness factor provides
253 a normalised value between 0 and 1, with 1 representing maximum groupiness of the wave
254 group envelope.
255
256 To better understand the infragravity wave characteristics on each of the platforms, it is
257 important to know the relative location of the data, within the surf zone. Throughout the TAT
258 dataset, H_{ss} decreases from the seaward-most to the shoreward-most sensor for every data
259 burst. This implies that the sea-swell wave breakpoint, through all tidal stages, is located in the
260 unsurveyed ~20 m zone between the seaward-most sensor and the platform edge, regardless of
261 the water depth over the platform. This is consistent with visual observations during the field
262 experiment, which indicate consistent sea-swell wave breaking at the platform edge (refer to
263 Figure **2b**). Therefore, it is assumed that the location of the sea-swell wave breakpoint x_b is at
264 the platform edge, 20 m seaward of the seaward-most sensor. The shoreward limit of the surf
265 zone (x = 0) was taken as the location where the water level at the shallowest sensor intersects
266 with the shoreline profile, and thus the normalized surf zone location x/x_b is obtained, where
267 x/x_b = 0 indicates the shoreline and x/x_b = 1 represents the seaward edge of the surf zone.

At LST, visual observation of the data revealed a clear initial shoreward increase in H_{ss} due to wave shoaling followed by a more rapid decay for the bursts close to high tide during all tides. Therefore, an average breaker coefficient γ_b, defined as H_{ss}/h at the onset of short wave breaking, was defined for each tide. The mean γ_b throughout all tides was 0.4. Using γ_b, data are given a normalised surf zone position h/h_b, where h_b is the water depth at the sea-swell wave break point defined as $h_b = H_b/\gamma_b$, where H_b is the breaking sea-swell wave height. Given that the profile at LST is quite linear in the region of the pressure sensors (refer to Figure **1c**), it is assumed that $x/x_b = h/h_b$.

2.4 XBeach modelling

Numerical modelling is used to complement the field data analysis and help with the interpretation of the results, as well as extending the parameter space beyond the conditions experienced during the field experiments. Modelling of the rock shore platform hydrodynamics was conducted using the phase-resolving (i.e., non-hydrostatic) variant of the widely used and open-source XBeach model (Roelvink et al., 2009). For the comparison between field measurments and model results, the model was set up using the surveyed intertidal profile, extending down to low water, and then extended to ensure the boundary conditions were in 15 m water depth. For TAT, the depth at the offshore ADCP was used to interpolate the bathymetry towards the platform edge where it was merged with the survey data, based on local knowledge. At LST, nearshore bathymetry was extracted from United Kingdom Hydrographic Office (UKHO) data, interpolated onto a regular grid and merged with the intertidal survey. When exploring the parameter space, idealised platform profiles were used and the model domain was extended to 20 m water depth to accommodate for peak wave

293 periods of up to 14 s. The sloping platform (LST) was simply represented by a single gradient
294 of 0.02 (1:50) extending 1000 m offshore to z = -20 m. The horizontal platform (TAT) was
295 represented by a 150-m wide section with a gradient of 0.005 (1:200), fronted by a steep 5-m
296 cliff with a gradient of 1, before extending offshore with the same gradient as the LST platform
297 to z = -20 m. Both idealised profiles were backed by a 5-m high cliff with a gradient of 1. The
298 profiles were constructed to resemble the natural profiles of Lilstock and Tatapouri, but with
299 identical landward and seaward sections to avoid biasing the model results.
300
301 The numerical model was first validated using field observations with the natural platform
302 profiles, and then used to generate an extended numerical data set for each of the field sites
303 using the idealised platform profiles. To generate the extended numerical dataset, a constant
304 water level was specified (SWL at the landward extend of the platforms; thus, at the base of
305 the cliff) and H_o and T_p were varied, with H_o ranging from 1 to 4 m at 1-m increments and T_p
306 ranging from 6 to 14 s at 2-s increments. The purpose of these model runs was to explore the
307 H_o-T_p parameter space beyond the field dataset and further examine the relationship between
308 the infragravity wave height H_{inf} and the wave power expression $H_o^2 T_p$. In these simulations,
309 the model was run using default parameters for a duration of 30 mins, with the initial 2 mins
310 used to allow the model to 'spin-up'. The modelled data were also decomposed into shoreward-
311 and seaward-propagating infragravity components as was done, for example, in a similar
312 numerical study of infragravity wave generation across coral reef platforms by Masselink et al.
313 (2019) using the methodology of Guza et al. (1984).
314
315 ## 3. Results
316
317 ### 3.1 Event summary

Wave conditions at the seaward-most sensors during the LST and TAT field experiments are presented in Figure **3**. At LST, the largest values of H_o were during the middle and latter half of the study period, during which H_o exceeded 1 m at high tide at the seaward-most sensor, with a maximum value of 1.91 m during tide 6. Peak wave periods ranged between 4 and 13 s, with a mean of 6.7 s. At TAT, H_o measured at the ADCP ranged between 0.59 and 1.57 m, peaking during tide 1 before decreasing for the remaining tides. Maximum and minimum peak wave periods were 7.8 s and 16.0 s, respectively, also peaking during tide 1. Mean H_{ss} and T_p at TAT were 0.92 m and 11.8 s, respectively.

Maximum H_{inf} on the LST platform was 0.34 m, measured at the shallowest sensor during tide 6 when H_o at the seaward-most sensor was largest. This is almost twice as large as the maximum H_{inf} measured on the TAT platform of 0.18 m. This was also measured at the shallowest sensor, although typically H_{inf} decreases across the TAT platform, but increases across the LST platform (discussed later). Furthermore, unlike at LST where the largest values of H_{inf} tend to coincide with the most energetic offshore forcing, H_{inf} at TAT shows little response to offshore forcing.

To investigate the infragravity wave energy level over the complete field survey period and its relationship with the offshore wave forcing at both sites, Figure **4** shows H_{inf} parameterized by the forcing parameter $H_o^2 T_p$ (following Inch et al., 2017), where H_o is the offshore wave height. The parameter $H_o^2 T_p$ is used as it is proportional to the offshore wave energy flux. To have a consistent value representing H_{inf} with which to relate to the offshore forcing conditions, H_{inf} is averaged over the surf zone (i.e., $0 < x/x_b < 1$) for each burst. To obtain

values of H_o, H_{ss} at the seaward-most sensor at LST during high tide conditions and the ADCP at TAT is deshoaled to a representative offshore water depth (20 m) using linear wave theory (ignoring wave refraction). Furthermore, data from LST are only included for bursts where $h > 3H_{ss}$ at the seaward-most sensor to ensure that the data are well outside the surf zone when deshoaled.

Data from LST show that H_{inf} is well predicted by $H_o^2 T_p$, with a linear regression revealing a coefficient of determination r^2 of 0.79 (Figure **4**). There is no evidence of infragravity saturation at LST as H_{inf} progressively increases with increasing $H_o^2 T_p$. These results are consistent with the findings of Inch et al. (2017) using data from a dissipative sandy beach, and other sandy beach studies that have indicated the importance of wave period in parameterizing infragravity energy in the nearshore (e.g., Ruessink, 1998; Senechal et al., 2011; Contardo and Symonds, 2013). In contrast, H_{inf} at TAT shows a very weak and barely significant relationship with $H_o^2 T_p$ (Figure **4**). The maximum $H_o^2 T_p$ value at TAT exceeds that of LST; yet, the corresponding H_{inf} is over 50% smaller at 0.11 m compared to 0.26 m at LST. There is also a strong indication that the infragravity wave motion at TAT is saturated for $H_o^2 T_p$ > 10.

3.2 Infragravity generation and propagation

To investigate the generation and propagation of infragravity waves on the two contrasting platforms in detail, two example data bursts were selected for further analysis. The bursts that were selected have a similar level of offshore forcing (Table **2**) and a good range of water depths throughout the surf zone.

Figure **5** shows the wave spectra at three different water depths on each platform, including the seaward-most sensor at LST and the ADCP at TAT, for the two data bursts. The sea-swell variance at LST is quite broad-banded and there is a slight decrease between h = 5.1 m (x/x_b = 1.83) and h = 1.8 m (x/x_b = 0.65), before becoming significantly less at h = 0.5 m (x/x_b = 0.19) (Figure **5a**). The infragravity variance displays the reverse of this trend, with a small increase between the two deepest sensors and a large increase to the shallowest sensor. The sea-swell variance at TAT is more narrow-banded at the ADCP location where h = 10.1 m (x/x_b = 1.77), but decreases and becomes less narrow-banded in shallower waters on the platform (Figure **5b**). The infragravity variance increases significantly between the ADCP and the platform at h = 1.5 m (x/x_b = 0.55), and then increases further at low infragravity frequencies (< 0.02 Hz), but decreases at high infragravity frequencies (> 0.02 Hz) at h = 0.6 m (x/x_b = 0.19).

Time series of the incident waves, wave groups and infragravity waves for different locations across the shore platforms for the two data bursts are illustrated in Figure **6a** and **b.** Compared to the seaward-most sensors at LST, waves at the ADCP at TAT are narrow-banded, clearly grouped, and fewer in number. Individual wave groups at LST can be traced through the shoaling zone into the outer surf zone before becoming indistinguishable. At TAT, while the wave groups are clear at the ADCP, the groupiness is much less defined on the platform. The increasing importance of infragravity waves in shallow water is quite clear at LST, but less so at TAT. Incident-wave statistics are shown in Figure **6c** and demonstrate that H_{ss} at TAT decreases very rapidly in the outer surf zone close to the platform edge, before decreasing steadily in the inner surf zone. In contrast, the dissipation of H_{ss} at LST is more rapid through the surf zone. As alluded to earlier, H_{inf} increases shoreward on the LST platform, but

392 decreases on the TAT platform, until the very inner surf zone where it increases (Figure **6d**).
393 Infragravity energy becomes increasingly important relative to sea-swell energy in shallower
394 water on both platforms, accounting for ~25% of the total variance at the shoreward-most
395 sensors (Figure **6e**).
396
397 Cross-correlation analysis was used to explore the infragravity wave generation mechanism for
398 the two data bursts at LST and TAT shown in Figure **6**. The cross-correlation between the wave
399 group envelope at the seaward-most sensors (PT15 at LST and the ADCP at TAT) and the
400 infragravity signal at all locations, and between the wave group envelope and infragravity
401 signal locally are both shown in Figure **7**.
402
403 At the seaward-most sensor on the LST platform, r_0 is significantly less than 0 indicating the
404 presence of a bound infragravity wave that is 180° out of phase with the wave groups. However,
405 the strongest negative correlation does not occur at zero time lag, but at a lag of 1.8 s, thus
406 implying that the trough of the bound infragravity wave lags behind the crest of the wave group
407 envelope. As the bound infragravity wave propagates shoreward towards the sea-swell wave
408 breakpoint, this lag grows to almost 5 s, as evidenced by the increased deviation away from the
409 predicted lag according to the wave group celerity C_g (Figure **7a**). The lag does not appear to
410 increase further in the surf zone where the bound wave continues to propagate shoreward
411 according to C_g, but the correlation weakens significantly in the inner half of the surf zone
412 (x/x_b < 0.5). The local cross-correlation between A and η_{inf} at LST (Figure **7b**) remains
413 negative at zero time lag from the seaward-most sensor all the way to the very inner surf zone
414 where there is some evidence of a switch from negative to positive correlation very close to
415 shore.
416

At TAT, there is also clear evidence of a bound infragravity wave at the ADCP location, as shown by the bar of strong negative (blue) correlation (Figure **7c**). Similar to LST, the strongest negative correlation occurs at a non-zero time lag of 4 s. Due to the lack of sensors on the platform edge, where sea-swell wave breaking occurs, as well as uncertainties regarding the exact bed profile shape between the ADCP and the seaward extent of the measured profile, calculation of the predicted lag was not attempted; therefore, the fate of the bound infragravity wave on reaching the platform cannot be determined using the field data alone and is investigated using numerical modelling later in the paper. However, in contrast to on the LST platform, the local cross-correlation between A and η_{inf} at TAT is positive at all locations on the platform, indicating that the infragravity wave and the wave group are in phase. This switch from negative to positive correlation suggests that the infragravity wave motion on the platform is generated using the breakpoint-forced mechanism, operating at the platform edge.

To assess whether the results from the two example data bursts presented in Figure **7** are representative for the two entire datasets, Figure **8a** and **b** shows the local cross-correlation coefficient at zero time lag for all locations and all bursts, relative to the normalized surf zone position. At LST, r_0 is almost entirely negative outside of the surf zone indicating that bound infragravity waves are dominant. The negative correlation increases towards the sea-swell wave breaking point and decreases across the surf zone. This can be interpreted as the bound infragravity waves being released as the sea-swell waves break and lose their group structure. Correlation becomes positive in the inner third of the surf zone, thus supporting the previous assertion that the correlation in Figure **7b** looked likely to switch from negative to positive close to shore. The relationship between bound infragravity waves and the sea-swell wave group is further elucidated by the corresponding groupiness factors presented in Figure **8c**. The

groupiness decreases in the outer surf zone following initial sea-swell wave breaking, and coinciding with the release of the bound infragravity waves, before rising rapidly in the inner surf zone to correspond with the switch to positive r_0.

The TAT data show that bound infragravity waves are prevalent at the ADCP, as indicated by the predominantly negative r_0 at this location. However, on the platform r_0 is mostly positive at all locations, as was also apparent in Figure **7d**. This provides further evidence that breakpoint-forced infragravity waves are dominant on the TAT platform as they are in phase with the sea-swell wave groups. The groupiness of the sea-swell waves at TAT increases significantly between the ADCP and the platform (Figure **8d**), perhaps as a result of strong shoaling on the platform slope. Unlike at LST, the groupiness decreases and is lowest in the inner surf zone. This is likely associated with the rapid dissipation of the sea-swell waves in the outer surf zone shortly after they have propagated onto the platform, as was shown in Figure **6c**.

3.3 XBeach modelling

The field results presented thus far have provided strong evidence that bound infragravity waves are dominant on the LST platform and, with slightly more reservations, that breakpoint-forced infragravity waves dominate the platform at TAT. To investigate this further, the non-hydrostatic (i.e., phase-resolving) version of the XBeach numerical model (Roelvink et al., 2009) was used.

The two example data bursts of field data shown in Figures **5**, **6** and **7** were used to help validate the XBeach model. It is emphasised that we do not seek to provide an extensive calibration of the numerical model as at both sites we do not have the appropriate wave boundary conditions

467 to force the model, nor do we have the complete bathymetry at the TAT site. Rather, the
468 comparison, presented in Figure **9**, serves to demonstrate qualitative agreement between the
469 field data and model results. The numerical model reproduces the observed shoreward decrease
470 in H_{ss} across the shore platform quite well at both LST and TAT (Figure **9c** and **g**).
471 Qualitatively, there is also good agreement between modelled and observed H_{inf}; however,
472 quantitatively the agreement is not great: H_{inf} is over-predicted by around 0.07–0.10 m for
473 LST (Figure **9d**) and by 0.03–0.05 m for TAT (Figure **9h**).
474
475 The modelled cross-correlation between the wave group envelope at the most seaward
476 coordinate and the infragravity time series at all locations for LST (Figure **9a**) closely mimics
477 what was seen in the field data (Figure **7a**). As was observed in the field data, the lag associated
478 with the strong band of negative (blue) correlation increases relative to the predicted lag as it
479 approaches the surf zone, reaching ~7 s at the outer edge of the surf zone. This suggests that
480 the trough of the bound wave lags behind the crest of the wave group by an amount that
481 increases as the sea-swell waves shoal prior to breaking. The local cross-correlation between
482 A and η_{inf} (Figure **9b**) also matches the field results (Figure **7b**) very well, remaining negative
483 at zero time lag throughout the model domain up until the very inner surf zone where it turns
484 to positive (Figure **9b**). This occurs because the infragravity wave crests increase the local
485 water depth allowing for larger sea-swell waves to exist whilst the smaller sea-swell waves
486 propagate in the infragravity wave troughs.
487
488 The modelled cross-correlation between the wave group envelope at the most seaward
489 coordinate and the infragravity time series at all locations for TAT is similar to LST outside
490 the surf zone, where a band of negative correlation indicates the presence of a bound
491 infragravity wave (Figure **9e**). This was also observed in the field data (Figure **7c**). Also, like

492 in the model run for LST, the bound infragravity wave lags increasingly behind the predicted
493 lag according to C_g, up to ~7 s at the platform edge. However, on reaching the shore platform,
494 the band of negative correlation associated with the bound infragravity wave rapidly weakens,
495 whilst a band of positive (red) correlation suddenly emerges in front of the wave group and
496 propagates towards the shore, by which time the bound infragravity waves has all but
497 disappeared (Figure **9e**). As with the field data from the TAT platform (Figure **7d**), the local
498 cross-correlation at zero time lag sees a rapid switch from negative to positive at the platform
499 edge (Figure **9f**), supporting the loss of the bound wave and introduction of a breakpoint-forced
500 infragravity wave. The outgoing infragravity wave, originating at the sea-swell wave
501 breakpoint is also characteristic of the breakpoint-forced mechanism.
502
503 Before presenting all model results across the full parameter space (H_o = 1–4 m; T_p = 6–14 s)
504 in the next section, Figure **10** shows the model output for an idealised sloping and horizontal
505 platform, for H_o = 4 m and T_p = 12 s. An identical wave signal was used in these two simulations
506 and a snapshot of the wave profiles across the topography, as well as the cross-shore variation
507 in mean sea level and significant wave height, are plotted in the upper panel of Figure **10**. For
508 both platforms there is a residual wave height at the base of the cliff. The two middle pairs of
509 panels shows the incoming and outgoing infragravity wave signal, derived using a lowpass
510 filter of T_p/4 and the method of Guza et al. (1984), and the lower pair of panels shows the cross-
511 shore variation in the total, incoming and outgoing significant infragravity wave height $H_{s,inf}$.
512 For the sloping platform (left panels) the incoming infragravity signal (assumed to be the bound
513 long wave based on previous results) progressively increases in amplitude towards the shore.
514 Part of the incoming signal reflects at the cliff, generating a less energetic outgoing infragravity
515 signal. The infragravity motion on the horizontal platform is more complex. There is still an
516 incoming bound long wave signal, but, at the submerged platform edge, the infragravity crests

become troughs on the platform, and the troughs become crests. As demonstrated earlier, this is the indicative of the time-varying breakpoint mechanism of infragravity wave generation. There are also two outgoing infragravity wave signals: one originating at the submerged platform edge (outgoing time-varying breakpoint wave) and one at the cliff at the landwards limit of the platform (reflection of the incoming time-varying breakpoint wave). The infragravity wave motion at the base of the cliff on the sub-horizontal platform ($H_{s,inf}$ = 1.5 m) is more energetic than that on the sloping platform ($H_{s,inf}$ = 1.2 m). The reduction in $H_{s,inf}$ at x = 100 m on the sloping platform and x = 150 m on the sub-horizontal platform is due to standing infragravity wave motion.

4. Discussion

4.1 Bound long wave versus breakpoint forcing

The numerical modelling results agree very well with the field data and indicate that the infragravity waves on the sloping platform (LST) have characteristics akin to those observed on dissipative beaches (e.g., Ruessink, 1998; Janssen et al., 2003; Inch et al., 2017), whilst infragravity wave observations on the sub-horizontal platform (TAT) agree well with those from steep beaches and coral reefs (e.g., Baldock, 2006; Lara et al., 2011; Pomeroy et al., 2012; Masselink et al., 2019). Furthermore, cross-correlation analysis between the infragravity motion across the shore platform and the wave groupiness seaward of the surf zone provides strong evidence that infragravity waves on the sloping platform are related to bound long waves whereas those on the sub-horizontal platform are breakpoint-forced long-waves. The key

distinguishing factor between the two mechanisms of infragravity wave generation is the gradient over which the incident waves shoal and break (e.g., Battjes et al., 2004), with a secondary role played by the incident wave steepness (e.g., Baldock and Huntley, 2002).

Baldock (2012) proposed a useful framework to enable an evaluation of the relative importance of the two mechanism through a surf beat similarity parameter $\xi_{surfbeat}$, which combines the normalised bed slope with the wave steepness as

$$\xi_{surfbeat} = \beta_{norm}\sqrt{\frac{H_b}{L_o}} \qquad (6)$$

where L_0 is the short-wave deep-water wave length, H_b is the wave height at the sea-well wave breakpoint and β_{norm} is the normalised bed slope as proposed by Battjes et al. (2004) as

$$\beta_{norm} = \frac{h_x}{\omega_{low}}\sqrt{\frac{g}{h_b}} \qquad (7)$$

where h_x and h_b are the beach slope and the depth at breaking, respectively, ω_{low} is the radian long-wave frequency, and g is the gravitational acceleration. Small and large values of $\xi_{surfbeat}$ favour the BLW and BFLW mechanism, respectively, with a $\xi_{surfbeat}$ value of 0.05–0.1 separating the two IG wave regimes (cf. Baldock, 2012, his Table 1; Contardo and Symonds, 2013, their Table **2**).

Inserting Eq. 6 into Eq. 7 yields

$$\xi_{surfbeat} = \left(1/\sqrt{2\pi}\right)\left(T_{IG}/T_p\right)\sqrt{\gamma}h_x \qquad (8)$$

where T_{IG} and T_p are the infragravity and incident wave period, respectively, and γ is the breaker criterion H_b/h_b. Assuming a typical IG-wave period T_{IG} of 4 times the incident-wave period T_p and an irregular breaker criterion of $H_b/h_b = 0.5$, Eq. 8 reduces to $\xi_{surfbeat} \approx 1.13h_x$, and $\xi_{surfbeat}$ is independent of the incident wave height or period. Finally, inserting a $\xi_{surfbeat}$ threshold of

562 0.05–0.1 separating the two IG wave regimes, following Baldock (2012) and Contardo and
563 Symonds (2013), results in a beach gradient threshold of 0.04–0.09. This implies that the bound
564 long wave mechanism can be expected to dominate on most sloping platforms, whose platform
565 gradient is always less than 0.1 and usually less than 0.05 (Trenhaile, 1999), whereas the
566 breakpoint-forced mechanism is expected to dominate sub-horizontal platforms as these
567 generally have a very steep low tide cliff and subtidal profile (Sunamura, 1992, Kennedy,
568 2015).
569
570 4.2 Which mechanism is most effective at generating infragravity waves?
571
572 Using data from the additional XBeach model runs with H_o = 1–4 m and T_p = 6–14 s, Figure
573 **11** illustrates the relationship between $H_{s,inf}$ and $H_o^2 T_p$ across this wide parameter space. The
574 LST and TAT field data are included in the plot, as well as field data collected from Perranporth
575 Beach, Cornwall, UK, from the study by Inch et al. (2017), to provide comparison with a
576 dissipative sandy beach. During the Perranporth field experiment, H_o ranged from 0.4 to 3.9 m
577 and T_p varied between 6 and 20 s; thus, conditions significantly more energetic than
578 experienced during the shore platform experiments. For all measured and modelled data sets,
579 $H_{s,inf}$ is averaged over the zone $0 < x/x_b < 0.33$ (i.e., inner third of the surf zone), hence the
580 notation $< H_{s,inf} >$ is used.
581
582 The model results for both rock platform sites are comparable and indicate that $< H_{s,inf} >$
583 increases rapidly for $H_o^2 T_p < 50$ m^2 s^{-1}, before increasing at a slower rate beyond this level. This
584 trend is replicated in the Perranporth field data, although the latter seem to plot somewhat below
585 the platform model results (note, however, that these are field measurements and not model
586 results). The field data from LST and TAT generally agree well with the model results;

587 however, they cover a very small parameter space ($H_o^2 T_p$ < 230 m^2 s^{-1}) and additional data from
588 both types of platforms under a greater range of forcing conditions is required to confirm the
589 model results.
590
591 The relationship between < $H_{s,inf}$ > and $H_o^2 T_p$ shown in Figure **11** for both sites suggests that a
592 linear parameterization of the infragravity wave height with the offshore forcing, as has often
593 been applied in previous studies, may not be suitable. The present results agree with those of
594 Senechal et al. (2011) who found that the best statistical predictor of infragravity runup on a
595 dissipative beach with a steep foreshore slope is not a linear fit, but rather a hyperbolic-tangent
596 function. Furthermore, a non-linear fit solves a common issue experienced when attempting to
597 fit a linear line to infragravity wave height or runup in which the linear line intercepts the
598 vertical axis at a value greater than 0. This is counter-intuitive as it implies that there is some
599 infragravity energy even when there is a complete absence of offshore forcing. The non-linear
600 curves fitted to the model results for LST and TAT, and the linear fit for Perranporth, plotted
601 in Figure **11**, describe the model data very well, with r^2 of 0.85, 0.79 and 0.94, respectively. It
602 must be emphasised, however, that these equations are highly site-specific (mainly dependent
603 on morphology and water level) and are not universally applicable.
604
605 The field observations at LST and TAT, and the supporting numerical model simulations,
606 strongly suggest that the potential for infragravity wave generation for sloping platforms is
607 similar to that for sub-horizontal platforms. This suggests that the bound long wave mechanism
608 of infragravity wave generation is as efficient as the breakpoint-forced mechanism. This is in
609 apparent contrast to the recent study of Masselink et al. (2019), who applied XBeach to model
610 wave transformation across coral reef platforms and concluded that the breakpoint-forced
611 mechanism is the more effective generator of infragravity energy, and that the most energetic

612 infragravity wave motion (normalised by incident wave motion) is generated on reef platforms
613 with a steep fore reef slope >1/6. There is, however, a fundamental difference between the
614 topographic profiles of coral reef and shore platform settings. Horizontal platforms are similar
615 to coral reefs with both characterised by a (sub)-horizontal platform fronted by a steep
616 submerged cliff; however, a sloping platform represents a continuous gradient and does not
617 have terminating (sub)-horizontal platform. Thus, in the continuously sloping platform case,
618 any BLW is able to 'grow' as it propagates across the sloping platform, whereas in the case of
619 a coral platform fronted by a low-gradient fore reef, the BLW is 'released' at the breakpoint
620 near the seaward edge of the reef platform. It is also worth pointing out that the water depth at
621 the base of fore reefs is generally much larger than at the base of the low tide cliff of sub-
622 horizontal shore platforms. Therefore, the characteristics of the infragravity wave motion
623 arriving at the different types of platforms are expected to be dissimilar. Clearly, some care has
624 to be exercised when transferring the current findings across to different coastal settings as site-
625 specific factors play a very significant role in the wave transformation and infragravity wave
626 generation processes.
627
628 4.3 Geomorphic implications
629
630 This paper provides the first detailed comparison of the different ways in which sloping and
631 sub-horizontal shore platforms filter the wave energy available for geomorphic work (erosion)
632 at the cliff toe. A unified conceptual framework for the origin of rock platforms is not yet
633 available: Trenhaile (1987, 1999) described the critical role of tidal range (sloping platforms
634 occur mainly in larger tidal ranges and sub-horizontal platforms occur mainly in micro-tidal
635 settings), whereas Sunamura (1992) distinguished both types in micro-tidal settings on the basis
636 of incident wave force and rock resistance: larger waves/weaker rock result in erosion of the

637 seaward edge of shore platforms and sloping platforms develop, whereas harder rocks/weaker
638 incident waves preserve or partially preserve the seaward edge, forming sub-horizontal
639 platforms. In the field, a clear demarcation between platform types is not always obvious and
640 recent modelling has demonstrated that different platform types can develop across a very
641 broad parameter space in which wave erosion and rock weathering processes variously
642 dominate (e.g., Matsumoto et al., 2018).
643
644 Regardless of formative demarcation conditions and the relative importance of wave and
645 weathering processes, our results highlight important differences in the wave regimes operating
646 on each platform type. Comparison of wave transmission across sloping and sub-horizontal
647 platforms, that are relatively similar in width and wave exposure, but different in terms of tidal
648 range, platform slope and the presence/absence of a steep seaward edge, suggest that sub-
649 horizontal platforms are more effective in filtering both incident and infragravity wave energy
650 and should therefore be characterised by lower wave energy levels at the emerged cliff toe.
651 Results further suggest contrasting mechanisms of infragravity wave generation on sloping and
652 sub-horizontal platforms. Overall the results are generally consistent with conceptual models
653 of shore platform development, but add important mechanistic understanding.
654 Recent reviews of rock platform development (Trenhaile 2018, 2019) emphasise the
655 importance of both wave erosion and weathering across the full spectrum of platforms. Under
656 stable sea level conditions platforms attain states of static equilibrium, and hence stable profile
657 morphology, due to wave erosion. During times of changing sea level, sloping shore platforms
658 are thought to evolve in dynamic equilibrium through shore-parallel cliff retreat and maintain
659 their general profile shape (e.g., Challinor, 1949; Trenhaile, 1974; Walkden and Dickson,
660 2008). Our results in a macro-tidal setting confirm that rapid tidal translation exposes the entire
661 surveyed width of the sloping platform surface to wave energy at incident frequencies, and that

662 the bound long wave mechanism dominates infragravity wave energy generation on these
663 surfaces, providing a mechanism for elevating water levels at the cliff toe. Whilst this elevates
664 the zone of maximum wave energy expenditure upwards and further landwards, which
665 increases the mechanical impact of short-period waves, enhances debris removal and enlarges
666 the spatial extent of the wetting and drying that leads to weathering, rock resistance also
667 remains important in setting the height of the cliff toe (cf. Trenhaile 2018). In contrast, sub-
668 horizontal platforms are thought to have declining rates of cliff recession through time (e.g.,
669 Sunamura, 1992), because platform gradients are reduced to a level where wave generated
670 shear stresses are below the erosional threshold. Continued cliff recession becomes possible
671 only through rock degradation accomplished by subaerial weathering processes and debris
672 removal by infragravity wave energy (Dickson et al., 2013). Our results confirm other studies
673 that show that sub-horizontal platforms are effective in filtering incident energy (e.g., Marshall
674 and Stephenson, 2011; Ogawa et al., 2011), and explain that the breakpoint-forced mechanism
675 is the likely source of infragravity wave energy on such platforms. As described above, the key
676 distinguishing factor between the two mechanisms of infragravity wave generation is the
677 gradient over which the incident waves shoal and break. Following Baldock (2012) and
678 Contardo and Symonds (2013), the threshold gradient is likely to be in the range 0.04 to 0.09.
679 Therefore the breakpoint-forced mechanism must clearly be the dominant source of
680 infragravity wave energy on shore platforms where a steep seaward edge (low-tide cliff) has
681 been preserved as a near-vertical cliff (e.g., Dickson, 2006). This paper shows that on sub-
682 horizontal platforms with partially preserved steep seaward edges developed in softer rocks
683 such as the silt- and sandstone at TAT the dominant mechanism of infragravity wave generation
684 remains breakpoint forcing.
685

686 It is interesting to contemplate that future sea-level rise may change the wave regime on sub-
687 horizontal shore platforms. While the relative elevation of the platform edge compared to the
688 tidal elevation remains important, as water levels rise, wave breaking may be less constrained
689 to the seaward edge and shift to parts of the shore platform that slope more gently. Hence,
690 increased water depth will not only increase the proportion of energy at incident and
691 infragravity wave frequencies that reaches the cliff toe (because less energy will be expended
692 on the platform edge), but it is also likely to switch the dominant mode of infragravity wave
693 generation to the bound long wave mechanism.
694
695 5. Conclusion
696
697 This paper set out to investigate and compare the generation and transformation of infragravity
698 waves on contrasting sloping and sub-horizontal shore platforms. Using field data from a
699 sloping platform at Lilstock, UK, and a sub-horizontal platform at Leigh, New Zealand,
700 complimented by numerical modelling (XBeach model), we have assessed the relative
701 importance of the bound wave and the time-varying breakpoint theories of infragravity wave
702 generation. Field measurements of wave transformation were collected over 8/6 tides, tide
703 range of 10.7/1.4 m and peak H_o = 1.91/1.57 m using 15/14 platform mounted pressure sensors,
704 for sloping/sub-horizontal platforms respectively.
705 The numerical modelling results strongly support the field data and indicate that infragravity
706 waves on sloping platforms have characteristics similar to those on dissipative beaches,
707 whereas infragravity wave observations on sub-horizontal platforms, align more closely with
708 steep beaches and coral reefs. Further cross-correlation analysis, between the infragravity
709 motion across the shore platform and the wave groupiness seaward of the surf zone, shows that

the group bound long wave mechanism is most important on sloping platforms, whereas breakpoint-forced long waves dominate on sub-horizontal platforms.

Further investigation shows the transformation of infragravity energy across the platforms is somewhat more energetic on sloping platforms than that on sub-horizontal platforms. This supports suggestions that sub-horizontal platforms provide better protection to coastal cliffs than their more steeply sloping counterparts. The model results support comparable studies from dissipative beaches that suggest a linear parameterization of the infragravity wave height with the offshore forcing, as has often been applied in previous studies, may not be suitable. The authors acknowledge that site-specific geomorphic factors including the elevation of the seaward terminus of the platform and the gradient are likely to play a key role in wave transformation. Further studies, where possible, should focus on in-situ field measurements to capture extreme wave conditions (H_s > 5 m) that can then be support further numerical simulations.

Acknowledgements

This research was funded by EPSRC grant EP/L02523X/1, Waves Across Shore Platforms, awarded to GM and MJA. We would like to thank our field and technical team: Peter Ganderton, Tim Scott, Olivier Burvingt, Pedro Almeida and Kate Adams. The data on which this paper is based are available from TP or via the online repository found at http://hdl.handle.net/10026.1/9105.

References

734 Baldock, T.E. 2006. Long wave generation by the shoaling and breaking of transient wave groups on a
735 beach. *Proceedings of the Royal Society of London A*, 462, 1853-1876.
736
737 Baldock, T.E. 2012. Dissipation of incident forced long waves in the surf zone – implications for the
738 concept of "bound" wave release at short wave breaking. *Coastal Engineering*, 60, 276-285.
739
740 Baldock, T.E., Huntley, D.A. 2002. Long-wave forcing by the breaking of random gravity waves on a
741 beach. *Proceedings of the Royal Society of London A*, 458, 2177-2201.
742
743 Battjes, J.A., Bakkenes, H.J., Janssen, T.T., van Dongeren, A.R. 2004. Shoaling of subharmonic gravity
744 waves. *Journal of Geophysical Research*, 109, C02009.
745
746 Becker, J.M., Merrifield, M.A., Yoon, H. 2016. Infragravity waves on fringing reefs in the tropical
747 Pacific: Dynamic setup. *Journal of Geophysical Research*, 121, 3010-3028.
748
749 Beetham, E.P., Kench, P.S. 2011. Field observations of infragravity waves and their behaviour on rock
750 shore platforms. *Earth Surface Processes and Landforms*, 36, 1872-1888.
751
752 Bertin, X., et al. (2018), Infragravity waves: From driving mechanisms to impacts, *Earth-Science*
753 *Reviews*, *177*, 774-799
754
755 Brander, R.W., Kench, P.S., Hart, D. 2004. Spatial and temporal variations in wave characteristics
756 across a reef platform, Warraber Island, Torres Strait, Australia. *Marine Geology*, 207, 169-184.
757
758 Cheriton, O.M., Storlazzi, C.D., Rosenberger, K.J. 2016. Observations of wave transformation over a
759 fringing coral reef and the importance of low-frequency waves and offshore water levels to runup,
760 overwash, and coastal flooding. *Journal of Geophysical Research*, 121, 3121-3140.
761

762 Contardo, S., Symonds, G. 2013. Infragravity response to variable wave forcing in the nearshore.
763 *Journal of Geophysical Research*, 118, 7095-7106.
764
765 Dickson, M. E. (2006), Shore platform development around Lord Howe Island, southwest Pacific,
766 *Geomorphology*, *76*(3), 295-315.
767
768 Dickson, M.E., Ogawa, H., Kench, P.S., Hutchinson, A. 2013. Sea-cliff retreat and shore platform
769 widening: steady-state equilibrium? *Earth Surface Processes and Landforms*, 38, 1046-1048.
770
771 Farrell, E.J., Granja, H., Cappietti, L., Ellis, J.T., Li, B., Sherman, D.J. 2009. Wave transformation
772 across a rock platform, Belinho, Portugal. *Journal of Coastal Research*, SI 56, 44-48.
773
774 Garrett, C.J.R., Toulany, B. 1981. Variability of the flow through the Strait of Belle Isle. *Journal of*
775 *Marine Research*, 39, 163-189.
776
777 Guza, R.T., Thornton, E.B., Holman, R.A. 1984. Swash on steep and shallow beaches. *Proceedings of*
778 *the 19th Conference on Coastal Engineering*. ASCE, New York.
779
780 Hasselmann, K. 1962. On the non-linear energy transfer in a gravity-wave spectrum: Part 1. General
781 theory. *Journal of Fluid Mechanics*, 12, 481-500.
782
783 Inch, K., Davidson, M., Masselink, G., Russell, P. 2017. Observations of nearshore infragravity wave
784 dynamics under high energy swell and wind-wave conditions. *Continental Shelf Research*, 138, 19-31.
785
786 Jager, T., 2016. Infra-gravity wave transformation across macrotidal rocky shore platforms.
787 Unpublished MSc thesis, Technical University Delft, The Netherlands.
788

789 Janssen, T.T., Battjes, J.A., Van Dongeren, A.R. 2003. Long waves induced by short-wave groups over
790 a sloping bottom. *Journal of Geophysical Research*, 108, 3252.
791
792 Jenkins, G.M., Watts, D.G. 1968. *Spectral analysis and its applications*. Holden-Day, San Francisco.
793
794 Kennedy, D. M. (2015), Where is the seaward edge? A review and definition of shore platform
795 morphology, *Earth-Science Reviews*, *147*, 99-108.
796
797 Kennedy, David M. (2016), The subtidal morphology of microtidal shore platforms and its implication
798 for wave dynamics on rocky coasts, *Geomorphology*, 268, pp. 146-158.
799
800 Lara, J.L., Ruju, A., Losada, I.J. 2011. Reynolds averaged Navier-Stokes modelling of long waves
801 induced by a transient wave group on a beach. *Proceedings of the Royal Society of London A*, 467,
802 1215-1242.
803
804 List, J.H. 1991. Wave groupiness variations in the nearshore. *Coastal Engineering*, 15, 475-496.
805
806 Longuet-Higgins, M.S., Stewart, R.W. 1962. Radiation stress and mass transport in gravity waves with
807 applications to 'surf beats'. *Journal of Fluid Mechanics*, 13, 481-504.
808
809 Lugo-Fernandez, A., Roberts, H.H., Wiseman Jr, W.J., Carter, B.L. 1998. Water level and currents of
810 tidal and infragravity periods at Tague Reef, St. Croix (USVI). *Coral Reefs*, 17, 343-349.
811
812 Marshall. R.J.E., Stephenson, W.J. 2011. The morphodynamics of shore platforms in a micro-tidal
813 setting: interactions between waves and morphology. *Marine Geology*, 288, 18-31.
814
815 Masselink, G. 1995. Group bound long waves as a source of infragravity energy in the surf zone.
816 *Continental Shelf Research*, 15, 1525-1547.

Masselink, G., Tuck, M., McCall, R., van Dongeren, A., Ford, M. and Kench, P., 2019. Physical and numerical modelling of infragravity wave generation and transformation on coral reef platforms. *Journal of Geophysical Research (Oceans) INCOMPLETE CITATION*.

Matsumoto, H., Dickson, M.E., Kench, P.S., 2018. Modelling the relative dominance of wave erosion and weathering processes in shore platform development in micro- to mega-tidal settings. *Earth Surface. Processes and Landforms*. 43, 2642-2653.

McCall, R., Masselink, G., Austin, M., Poate, T. and Jager, T., 2017. Modelling incident-band and infragravity wave dynamics on rocky shore platforms. *Proceedings Coastal Dynamics*, ASCE, Helsingor, Denmark, 1658-1669.

Nutall, A.H. 1971. *Spectral estimation by means of overlapped FFT processing of windowed data*. Naval Underwater Systems Center (NUSC) Report No. 4169. New London, Connecticut.

Ogawa, H., Dickson, M.E., Kench, P.S. 2011. Wave transformation on a sub-horizontal shore platform, Tatapouri, North Island, New Zealand. *Continental Shelf Research*, 31, 1409-1419.

Ogawa, H., Dickson, M.E., Kench, P.S. 2015. Hydrodynamic constraints and storm wave characteristics on a sub-horizontal platform. *Earth Surface Processes and Landforms*, 40, 65-77.

Pequignet, A.C.N., Becker, J.M., Merrifield, M.A., Aucan, J. 2009. Forcing of resonant modes on a fringing reef during tropical storm Man-Yi. *Geophysical Research Letters*, 36, L03607.

Pequignet, A.C.N., Becker, J.M., Merrifield, M.A. 2014. Energy transfer between wind waves and low-frequency oscillations on a fringing reef, Ipan, Guam. *Journal of Geophysical Research*, 119, 6709-6724.

Poate, T., Masselink, T., Austin, M., Dickson, M., Kench, P. 2016. Observations of wave transformation on macro-tidal rocky platforms. *Journal of Coastal Research*, SI75, 602-606.

Poate, T., Masselink, G., Austin, M.J., Dickson, M., McCall, R. 2018. The role of bed roughness in wave transformation across sloping rock shore platforms. *Journal of Geophysical Research*, 123, 97-123.

Pomeroy, A., Lowe, R., Symonds, G., van Dongeren, A., Moore, C. 2012. The dynamics of infragravity wave transformation over a fringing reef. *Journal of Geophysical Research*, 117, C11022.

Roelvink, D., Reniers, A., van Dongeren, A., van Thiel de Vries, J., McCall, R., Lescinski, J. 2009. Modelling storm impacts on beaches, dunes and barrier islands. *Coastal Engineering*, 56, 1133-1152.

Ruessink, B.G. 1998. The temporal and spatial variability of infragravity energy in a barred nearshore zone. *Continental Shelf Research*, 18, 585-605.

Ruju, A., Lara, J.L., Losada, I.J. 2012. Radiation stress and low-frequency energy balance within the surf zone: a numerical approach. *Coastal Engineering*, 68, 44-55.

Senechal, N., Coco, G., Bryan, K.R., Holman, R.A. 2011. Wave runup during extreme storm conditions. *Journal of Geophysical Research*, 116, C07032.

Stephenson, W. J., Dickson, M. E., & Denys, P. H. (2017). New insights on the relative contributions of coastal processes and tectonics to shore platform development following the Kaikōura earthquake. Earth Surface Processes and Landforms, 42(13), 2214-2220.

Sunamura, T. 1992. *Geomorphology of rocky coasts*. Wiley, New York.

Symonds, G., Huntley, D., Bowen, A.J. 1982. Two-dimensional surf beat: long wave generation by a time-varying breakpoint. *Journal of Geophysical Research*, 87, 492-498.

Trenhaile, A.S. 1974. The geometry of shore platforms in England and Wales. Transactions of the Institute of British Geographers 62, 129–142.

Trenhaile, A.S. 1987. *The geomorphology of rock coasts*. Oxford University Press, Oxford.

Trenhaile, A.S. 1999. The width of shore platforms in Britain, Canada, and Japan**.** *Journal of Coastal Research*, 15, 355-364.

Trenhaile, A.S. 2018. Shore platform erosion and evolution: Implications for cosmogenic nuclide analysis, *Marine Geology*, 403, 80–92.

Trenhaile, A.S. 2019. Hard-Rock Coastal Modelling: Past Practice and Future Prospects in a Changing World, *Journal of Marine Science and Engineering*, 7, 34, 1-16.

Van Dongeren, A., Battjes, J., Janssen, T., van Noorloos, J., Steenhauer, K., Steenbergen, G., Reniers, A. 2007. Shoaling and shoreline dissipation of low-frequency waves. *Journal of Geophysical Research*, 112, C02011.

Van Dongeren, A., Lowe, R., Pomeroy, A., Trang, D.M., Roelvink, D., Symonds, G., Ranasinghe, R. 2013. Numerical modelling of low-frequency wave dynamics over a fringing coral reef. *Coastal Engineering*, 73, 178-190.

Walkden, M.J.A, Dickson, M.E. 2008. Equilibrium erosion of soft rock shores with a shallow or absent beach under increased sea level rise. Marine Geology 251: 75–84.

902

Figure 1. Location maps and aerial images of LST (a) and TAT (b). Red dashed lines indicate the location of the instrument arrays across the intertidal platforms. Cross-shore profile of the platform at LST (c) and TAT (d). Black dots are the pressure sensor locations and the vertical black bars indicate the local tidal range. The standard deviation (std) of the profile surface is provided as an indication of relative roughness. Note the different axis limits. Dashed line indicates un-surveyed section of profile.

Figure 2. Site photos at low tide and high tide at TAT (a and b) and LST (c and d).

Figure 3. Summary wave conditions during the two field experiments: significant sea-swell wave height H_o (a and b), peak wave period T_p (c and d), and water depth h (e and f) at LST (left panels) and TAT (right panels). Mean depth across platform at LST = 4.2 m and TAT = 0.95 m. Data shown are from the seaward-most PT at LST and the ADCP at TAT. Vertical dashed lines indicate burst times used for subsequent analysis. Note the different axis limits between e and f.

Figure 4. Infragravity wave height H_{inf} averaged across the surf zone versus $H_o^2 T_p$ at LST (circles) and TAT (dots). Black lines are best-fit linear regression lines with coefficients of determination r^2 given in the figure.

Figure 5. Wave spectra at three different water depths, as indicated in the figure legend, at LST (a) and TAT (b). Vertical dashed line indicates the transition between infragravity and sea-swell frequencies at 0.05 Hz. A 95% confidence bar is given in the figure.

Figure 6. Example sea-swell (black), infragravity (red), and wave group envelope (blue) time series of 180 s for LST (a) and TAT (b). The time series are stacked from the seaward-most (top) to the landward-most (bottom) and are offset for clarity. The horizontal dashed lines indicate the seaward edge of the surf zone. Sea-swell wave height H_{ss} (c), infragravity wave height H_{inf} (d), percentage of total wave variance in the infragravity band IG % (e), and water depth h (f), versus normalized surf zone location x/x_b at LST (circles) and TAT (dots). Vertical dashed lines indicate the sea-swell wave breakpoint at x/x_b = 1.

Figure 7. Cross-correlation between the wave group envelope at the seaward-most sensor (PT15 at LST and the ADCP at TAT) and the infragravity time series at all sensors (a and c), and cross-correlation between the wave group envelope and the infragravity time series at each sensor (b and d) at LST (top panels) and TAT (bottom panels). Vertical solid lines indicate a time lag of 0 s and horizontal dashed lines indicate the sea-swell wave breakpoint at x/x_b = 1. The dotted line in a is the predicted time lag for an incident wave propagating at the wave group celerity C_g. Red indicates positive correlations and blue indicates negative correlations.

Figure 8. Correlation coefficient at zero time lag r_0 between the wave group envelope and the infragravity time series (a and b), and groupiness factor GF (c and d), versus normalised surf zone location x/x_b for all locations during all bursts at LST (left panels) and TAT (right panels). Boxplots are overlain representing the data in x/x_b bins of 0.1. On each box, the central line is the median value and the upper and lower bounds are the 75th and 25th percentiles, respectively.

Figure 9. Cross-correlation between the wave group envelope at the most seaward coordinate and the infragravity time series at all locations (a and e), and cross-correlation between the wave group envelope and the infragravity time series at each location (b and f). Red indicates positive correlations and blue indicates negative correlations. Comparison between modelled (black dots) and measured (red dots) sea-swell wave height H_{ss} (a and g) and infragravity wave height H_{inf} (g and h). Results are from XBeach-G model runs simulating LST (top panels) and TAT (bottom panels) using the same forcing conditions as in Figure **7**. Note the different axis limits.

Figure 10. Numerical model results output for idealised sloping (left panels) and horizontal (right panels) platform, for H_o = 4 m and T_p = 12 s. Idealised platform profile and cross-shore variation in example wave profile, mean sea level and significant wave height (a and b). Incoming and outgoing infragravity wave signal with colourmap running from -0.7 m (blue) to +0.7 m (red), (c, d, e and f). Total, incoming and outgoing significant infragravity wave height $H_{s,inf}$, (g and h).

Figure 11. Infragravity wave height $< H_{s,inf} >$ averaged over the inner surf zone ($0 < x/x_b < 0.33$) versus $H_o^2 T_p$ for measured (markers) and modelled (lines) data at LST and TAT, and measured data from Perranporth Beach (PPT), UK, from Inch et al. (2017).

962 **Table 1.** Summary statistics for the LST and TAT field experiments.

963 **Table 2.** Offshore wave conditions during two example data bursts at LST and TAT.

964

965

966

967

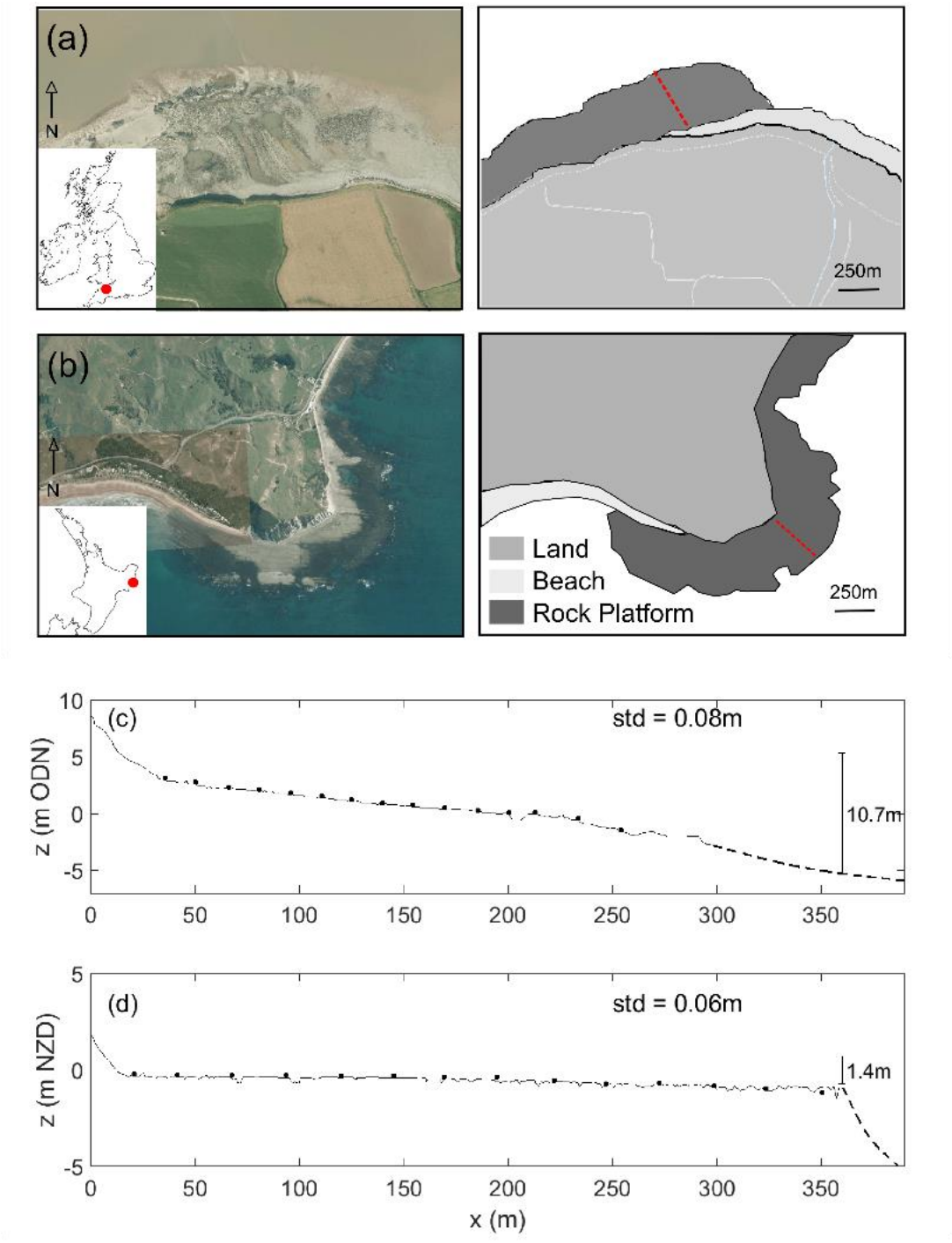

968

969 Figure 1

970 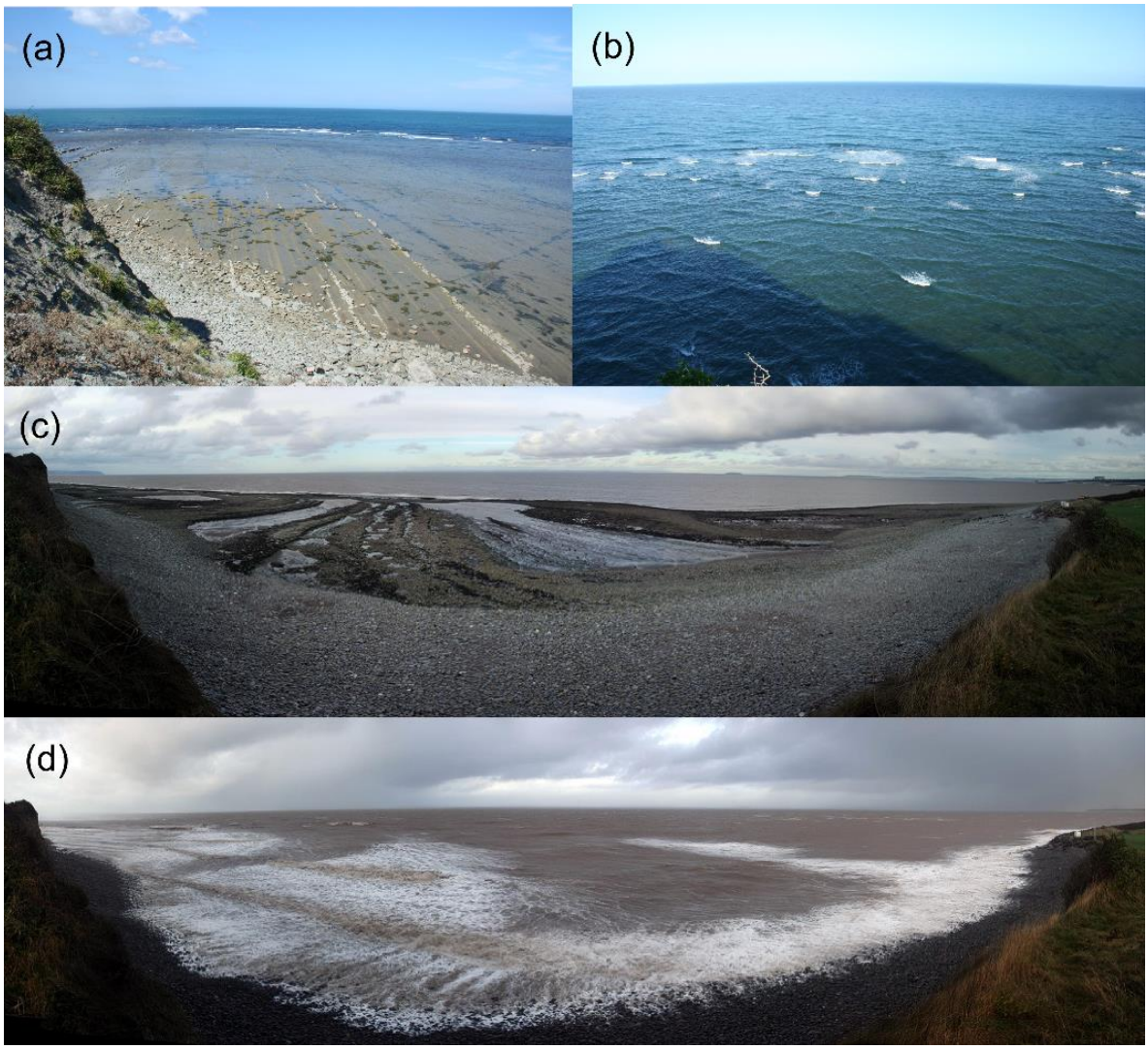

971 Figure 2

972

973 Table 1

Parameters		LST	TAT
Deployment data	Duration (tides)	8	6
	# PTs	15	14
	PT spacing (m)	~15	~25
	PT *z* range (min, max) m ODN, m NZD	-1.46, 3.14	-1.18, -0.22
	PT *x* range (m)	225	325
Platform morphology	Intertidal platform width (m)	325	340
	Bedrock	Mudstone	Siltstone
	Average tanβ between PTs	0.021	0.0004
	Mean spring tide range, mean low water spring (m)	10.7, -5	1.4

974 Note: PT = pressure sensor, tanβ = slope, ODN – ordnance datum Newlyn, NZVD = New
975 Zealand Vertical Datum.

976

977

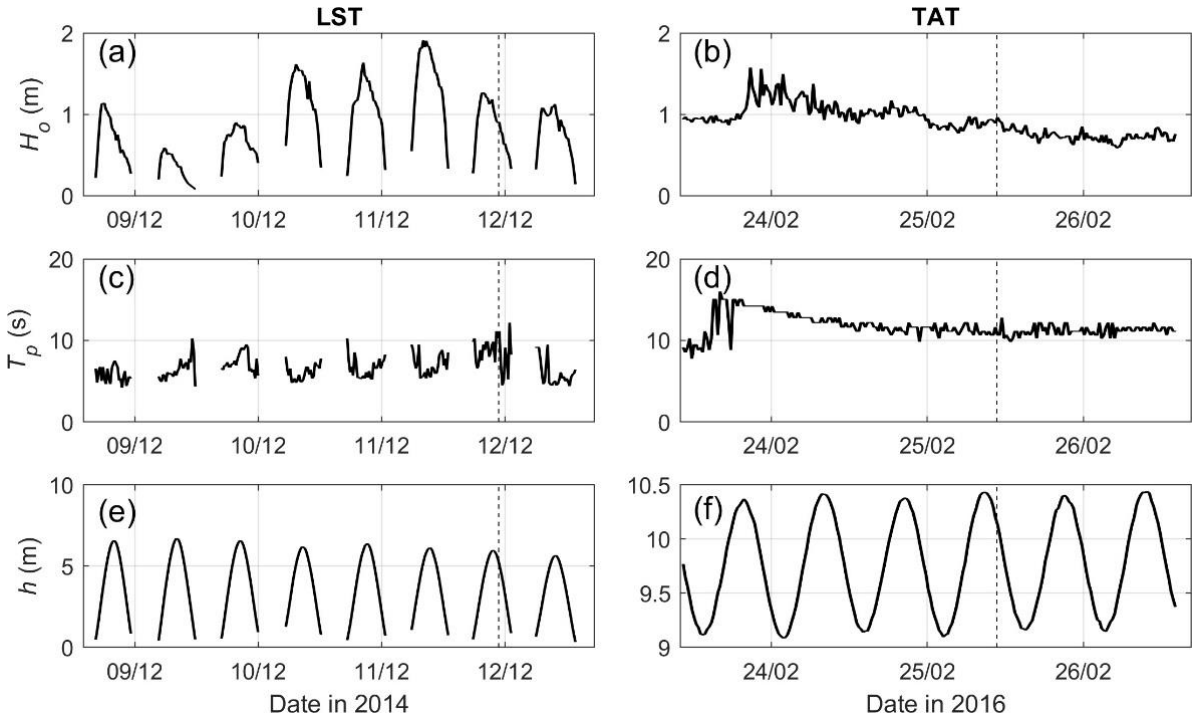

978

979 Figure 3

980

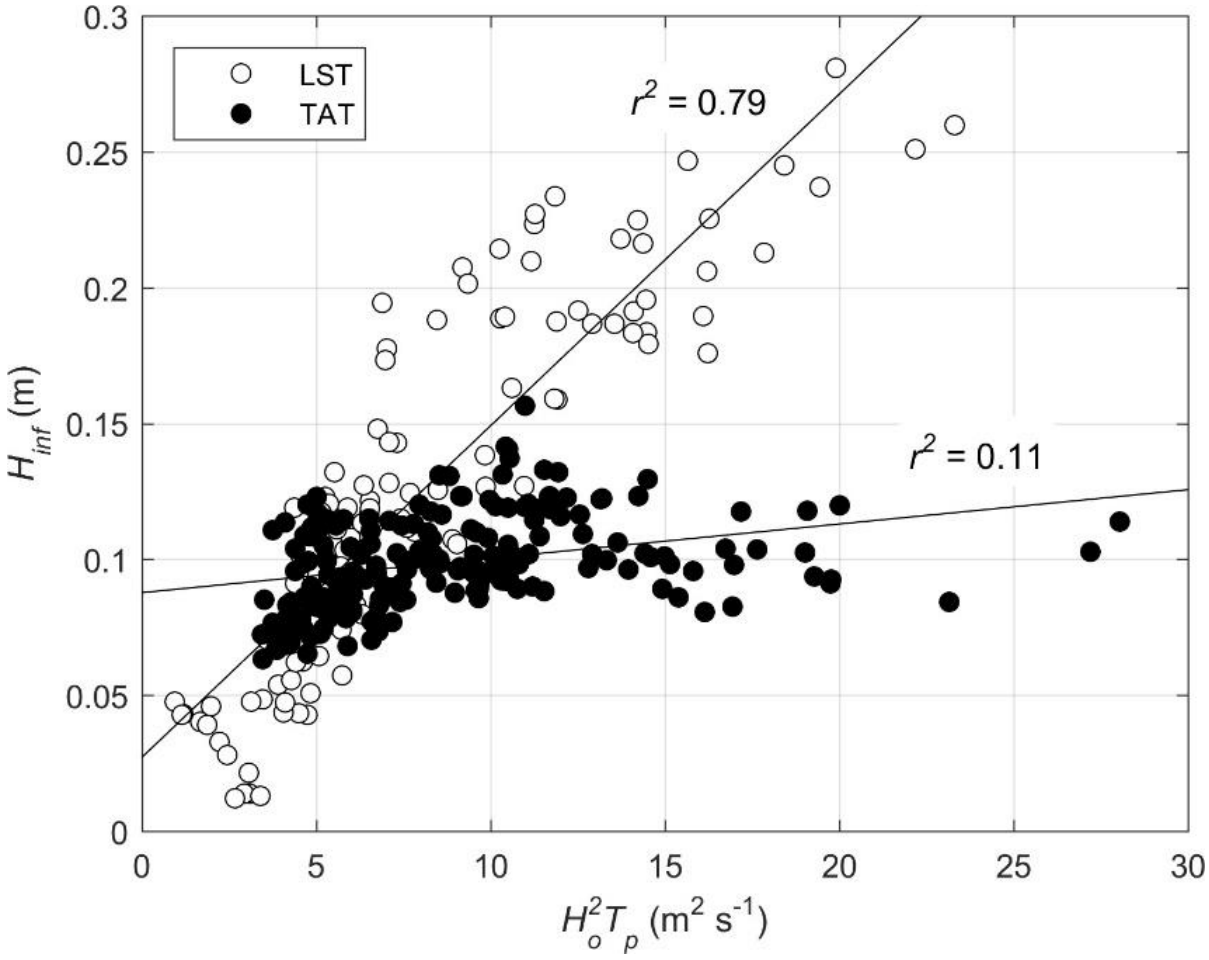

981

982 Figure 4

983

	H_o (m)	T_p (s)	$H_o^2 T_p$ ($m^2 s^{-1}$)
LST	0.81	11.1	7.30
TAT	0.90	10.7	8.59

984 Table 2

985

986

987

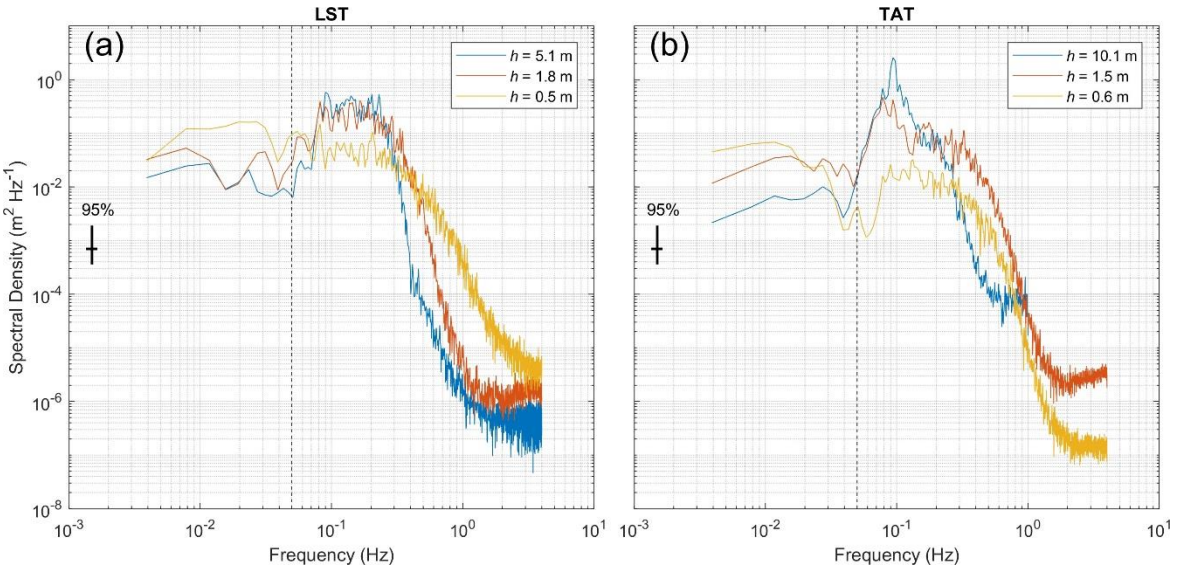

988

989 Figure 5

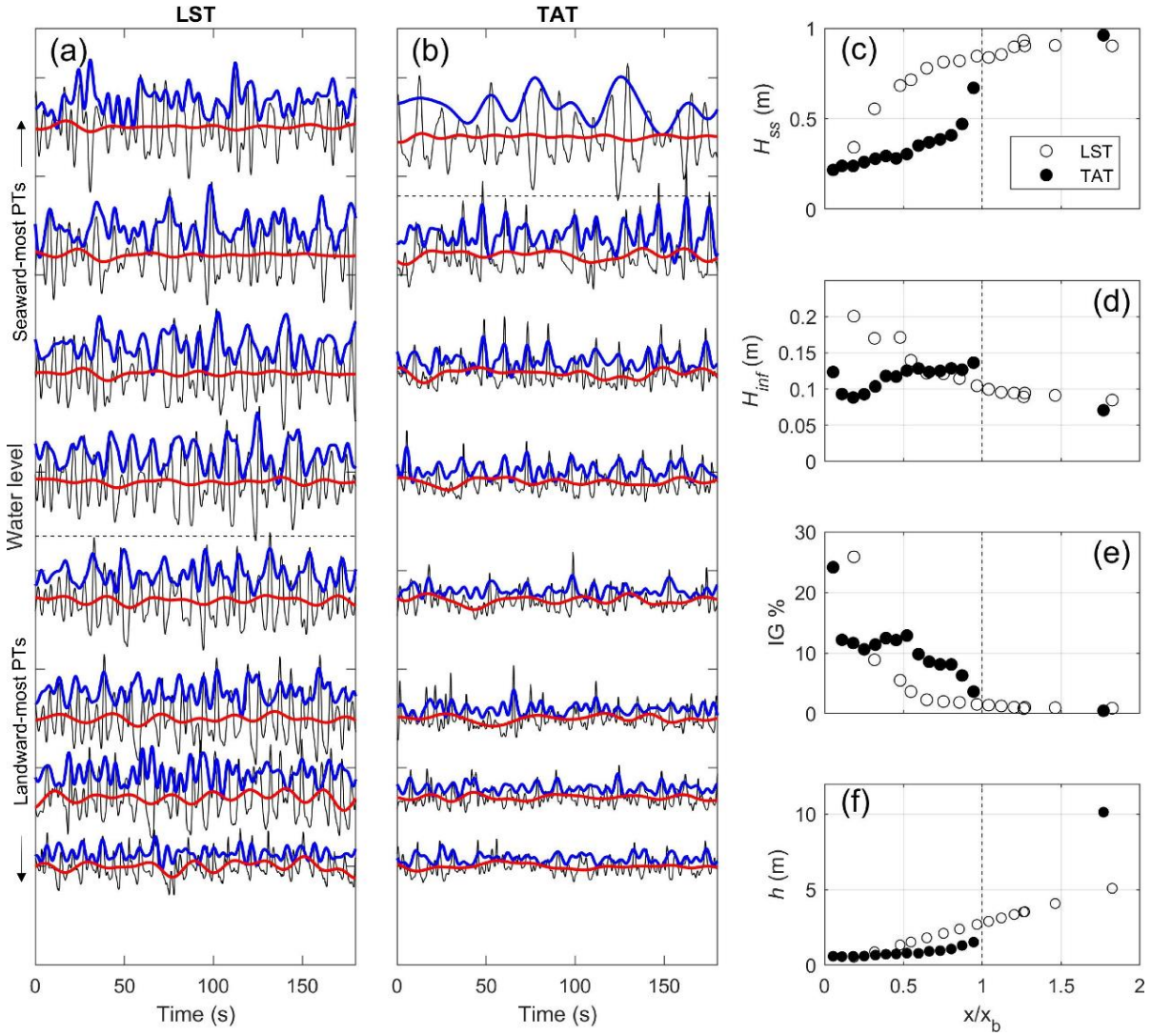

990

991 Figure 6

992

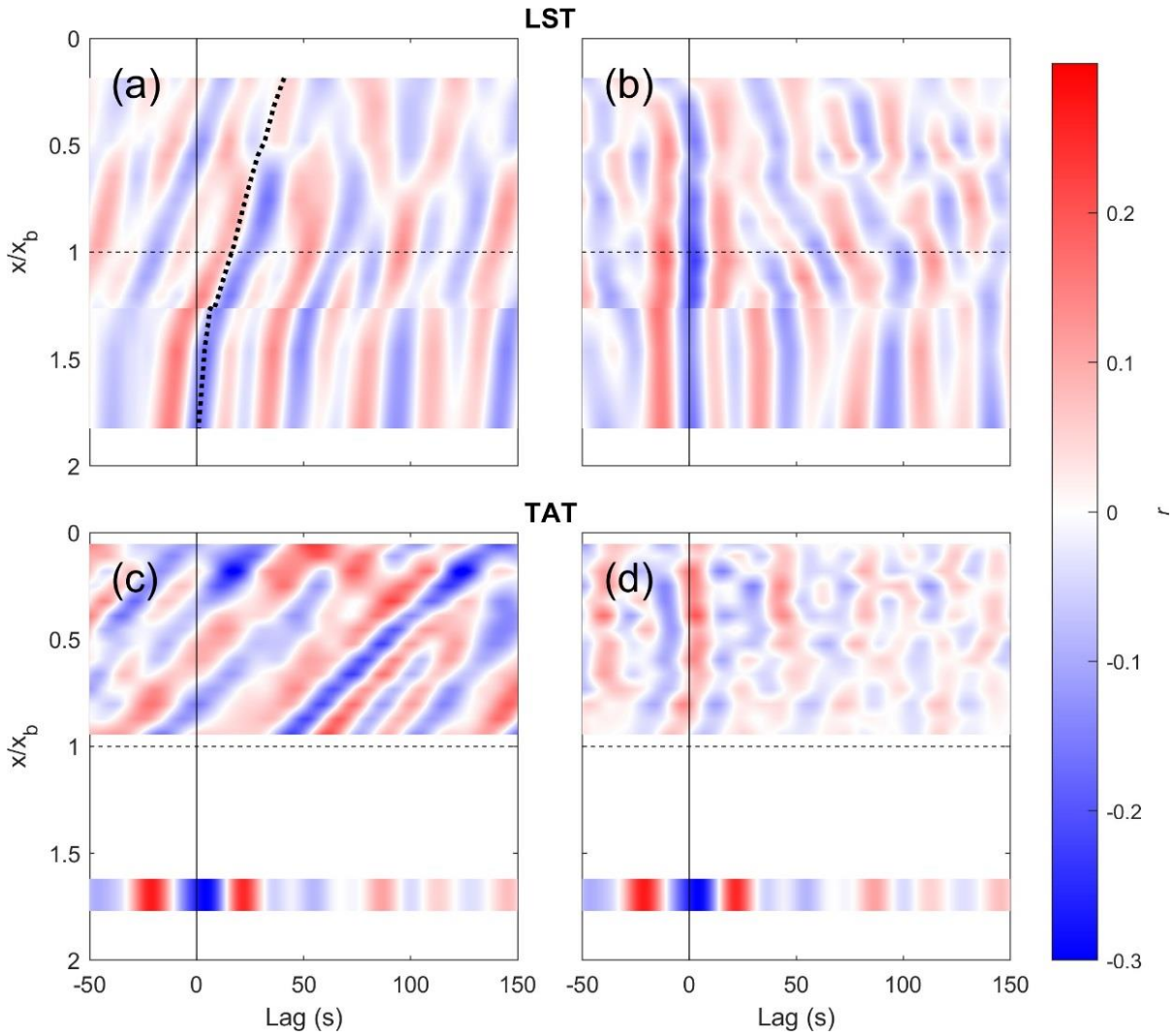

993

994 Figure 7

995

996

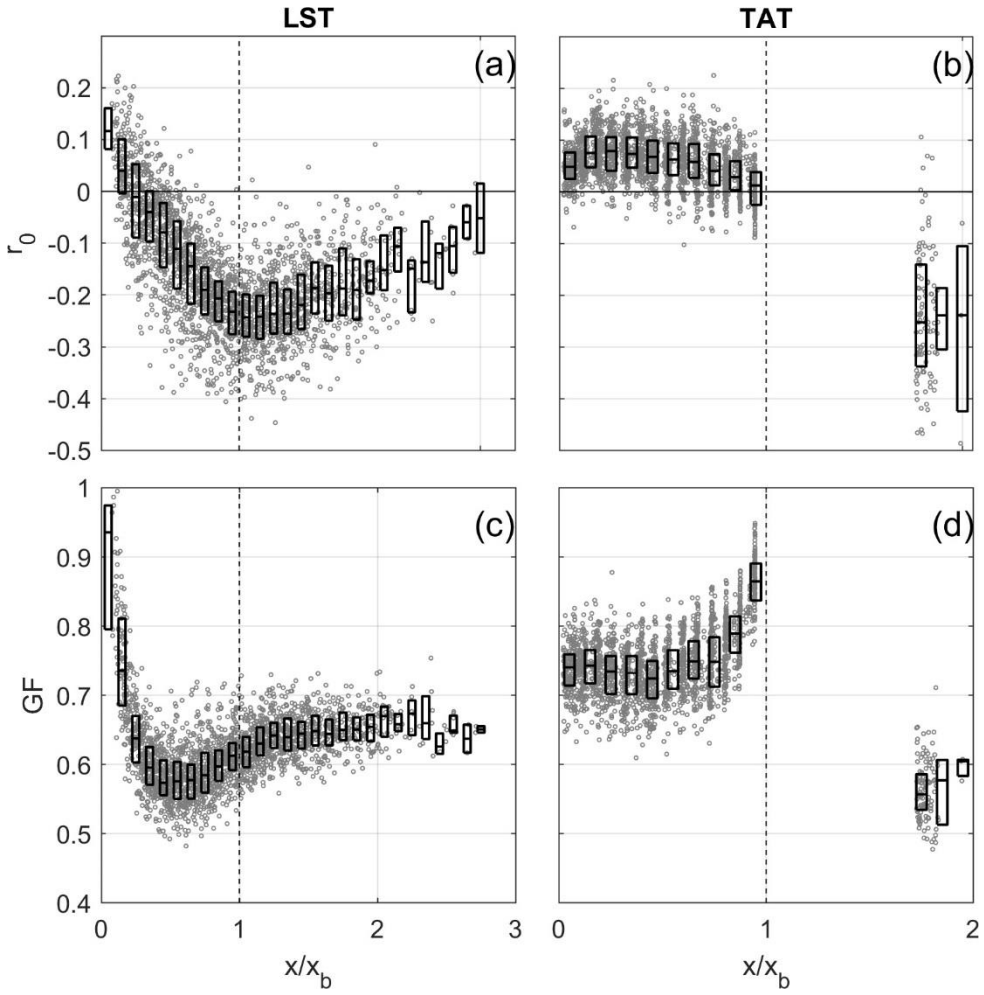

997

998 Figure 8

999

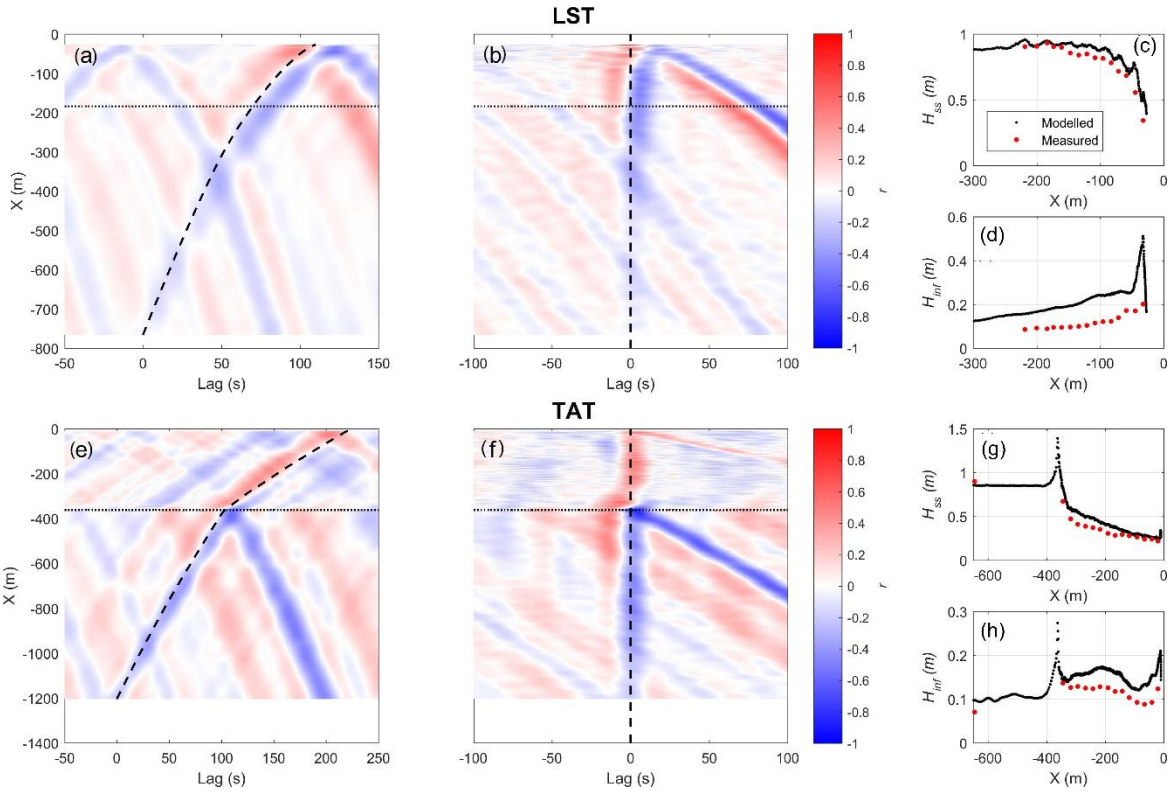

1000

1001 Figure 9

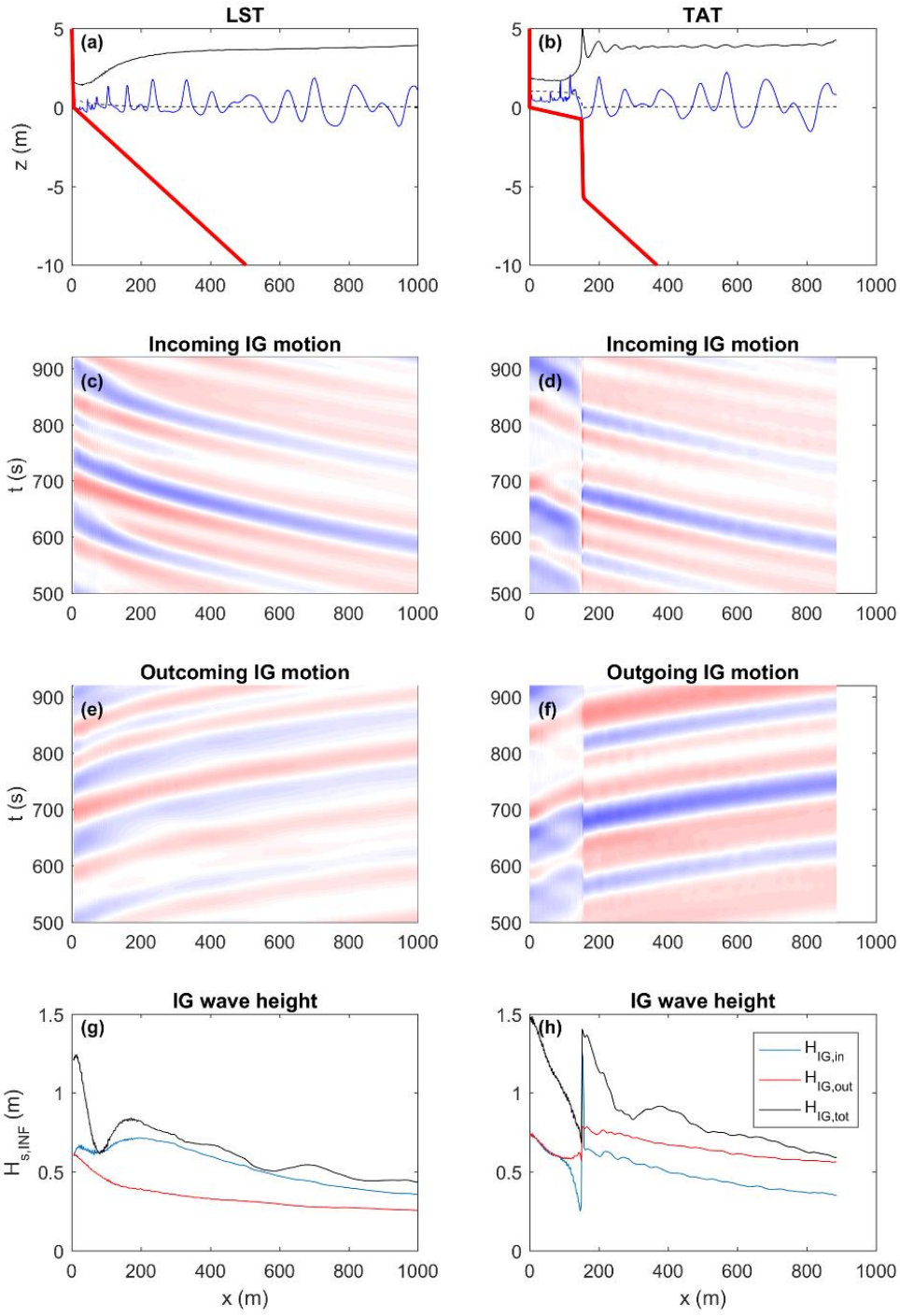

1002

1003 Figure 10

1004

1005

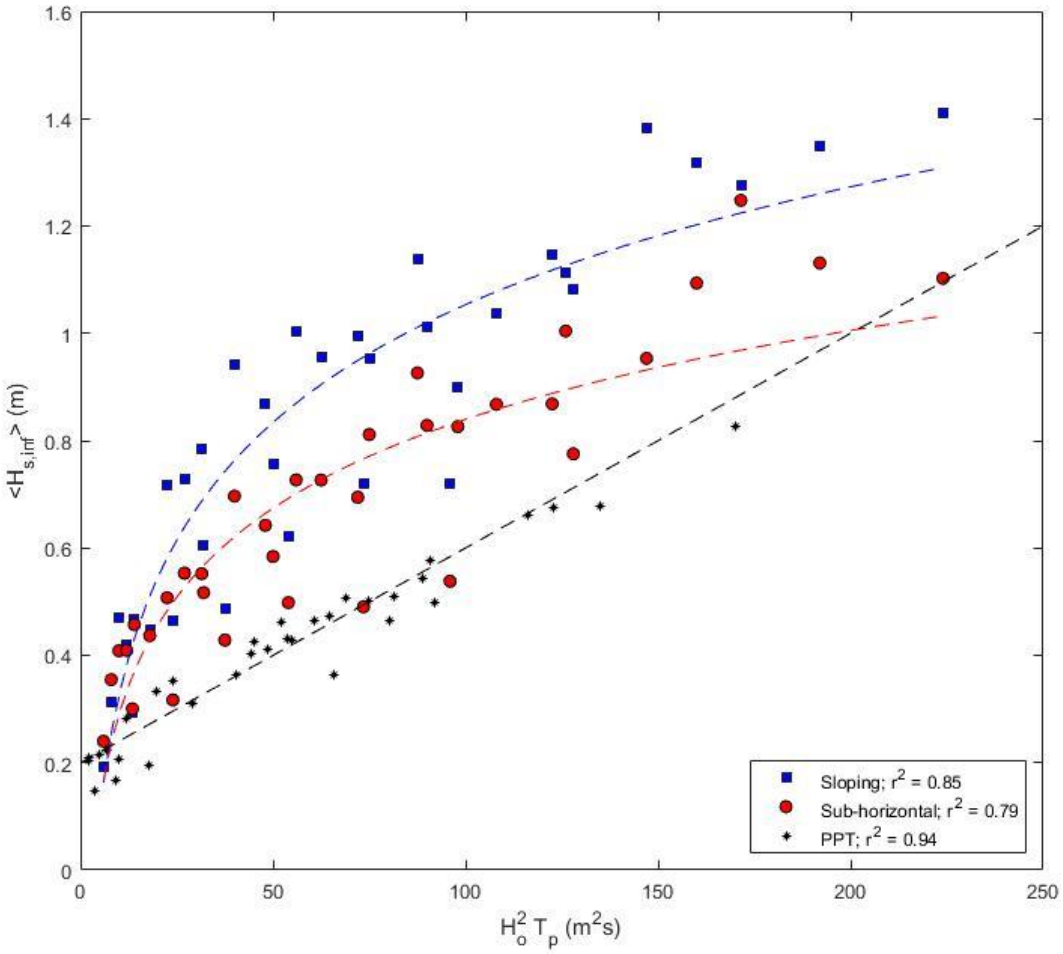

1006

1007 Figure 11